stellarator news

Published by Fusion Energy Division, Oak Ridge National Laboratory
Building 5700 P.O. Box 2008 Oak Ridge, TN 37831-6169, USA

Editor: James A. Rome Issue 105 September 2006
E-Mail: jar@ornl.gov Phone (865) 482-5643
On the Web at *http://www.ornl.gov/sci/fed/stelnews*

Turbulence measurements and anomalous transport modeling in HSX

Recent HSX experimental results have demonstrated the reduction of neoclassical particle and thermal transport in a quasi-helically symmetric (QHS) configuration as compared to a configuration with the quasi-symmetry intentionally degraded (Mirror) [1]. The total transport in both configurations is larger than neoclassical predictions across most of the plasma minor radius, becoming increasingly anomalous towards the edge. Because turbulence is typically assumed to be the source of anomalous transport in magnetic confinement devices, multiple Langmuir probes have been used to investigate the structure of electrostatic turbulence in the edge of both the QHS and Mirror configurations. The following measurements and analyses are performed for **B** = 0.5 T, 50-kW electron cyclotron resonance heating (ECRH) discharges in both the QHS and non-symmetric Mirror configurations.

Large fluctuation levels, typical of a turbulent environment, are observed in the edge plasma of HSX discharges. Figure 1 shows the normalized ion saturation current fluctuation levels ($\tilde{I}_{\mathrm{sat}}/\langle I_{\mathrm{sat}}\rangle$) in both the QHS and Mirror configurations. They are as large as 40% at the separatrix, and are very similar between the two configurations at these operating conditions. Normalized floating potential fluctuations ($e\tilde{\varphi}_{\mathrm{float}}/\langle T_e\rangle$) are comparable in magnitude, as predicted by linear electron drift wave theory. Also shown in the shaded region is a range of mixing length estimates [$\tilde{n}/n = (3-10)\rho_s/L_n$] within which many previous experiments have reported similar fluctuation levels (e.g., Ref. [2]).

Conditional averaging was used to develop two-dimensional (2D) correlation functions of both ion saturation current and floating potential. This was accomplished using a 16-pin linear ("poloidal") probe array, moved radially on a shot-by-shot basis, in conjunction with a second, fixed reference probe tip displaced toroidally.

In this issue . . .

Turbulence measurements and anomalous transport modeling in HSX
Langmuir probes have been used to characterize the structure of edge turbulence in both quasi-helically symmetric and non-symmetric configurations in HSX. Measured features (fluctuation levels, correlation lengths, crossphases) are similar in the two configurations under present operating conditions and reveal some consistency with theoretical electron drift wave predictions. **1**

Density regime of complete detachment and operational density limit in LHD
High volume-averaged density of 3.5 times as high as the Sudo scaling has been achieved using pellet injection in the Large Helical Device, where the density profile is strongly peaked. Even in these pellet-fueled plasmas, the edge densities are similar to those in gas-fueled plasmas. Complete detachment in LHD takes place when the edge temperature at the LCFS decreases to a critical value of ~100 eV. The critical edge density that results in complete detachment is proportional to the square root of the heating power, as is expressed in the Sudo density limit scaling. **4**

NCSX component production hits its stride
Modular coil and vacuum vessel segments are being delivered. Modular and toroidal field coil fabrication will continue throughout 2007. Sub-assembly activities have begun and will continue through 2008 as more finished components become available. The device will be installed, adapted to power supplies and controls, and tested by creating a first plasma in 2009. **8**

Stellarator reactor design presentation materials available
The lectures by Horst Wobig are available on the W7-AS Web site. **9**

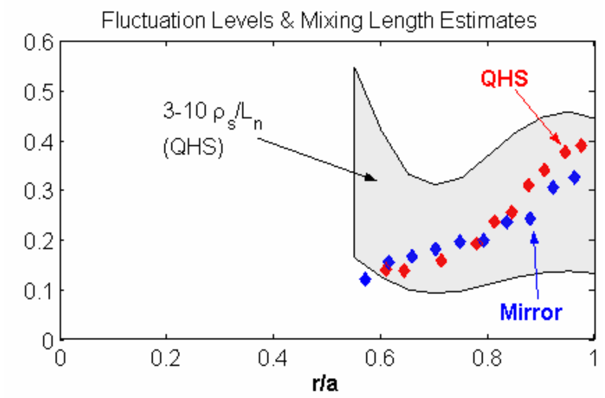

Fig. 1. Normalized ion saturation current fluctuation levels in both QHS and Mirror configurations. The shaded region indicates a range of common mixing-length estimates.

Figure 2 shows contours of the 2D correlation function (at a constant time lag) developed over a number of discharges for ion saturation current in the QHS configuration at a line-averaged density $\langle n_e \rangle$ of 1.0×10^{12} cm^{-3}. These data were acquired just inside the separatrix. The characteristic poloidal and radial scale lengths are ~1.5 cm in both directions. A similar structure is seen in the floating potential measurements, with no substantial spatial separation in the peak correlation. This is indicative of the drift wave nature (near-zero n-φ cross phase) of the turbulence.

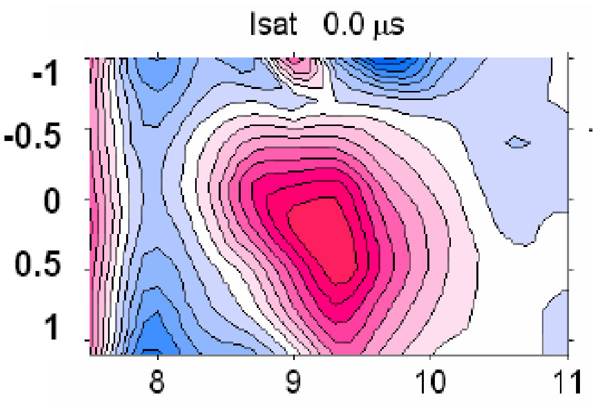

Fig. 2. 2D correlation function of ion saturation current in the QHS configuration. The radial and vertical (poloidal) axes are in centimeters.

Shown in Fig. 3 are the radial correlation lengths in both QHS and Mirror configurations for a number of discharges with varying line-averaged densities. Each data point shown here is obtained in a single shot through the use of two radially separated probe tips. The radial correlation length decreases with increasing density. A limited number of swept Langmuir probe measurements have indicated a decrease in the edge electron temperature T_e with increasing $\langle n_e \rangle$. This would be consistent with turbulence structure sizes scaling with the local value of ρ_s ($\sim T_e^{1/2}$), as expected in local drift wave theory. Furthermore, the poloidal scale length is comparable to the radial scale length as seen in the 2D correlation functions, with $k_\theta \rho_s \sim 0.15$. Again, the scale lengths are nearly identical in the QHS and Mirror configurations under these operating conditions.

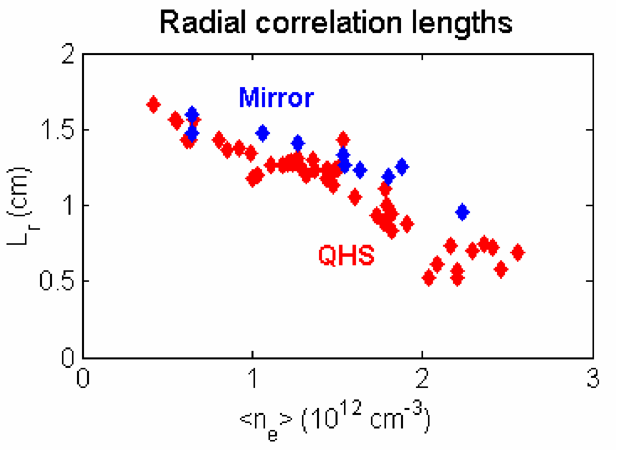

Fig. 3. Radial correlation lengths in both QHS and Mirror configurations.

To estimate the particle transport driven from the measured fluctuations, the cross phase between potential and density is required. Using established spectral analysis techniques [3], the spectra of n-φ cross phase, $\alpha_{n\varphi}(\omega)$, and local poloidal wave number, $k_\theta(\omega)$, are calculated. Figure 4 shows a contour plot of the joint distribution of $\alpha_{n\varphi}$ vs k_θ, conditioned on frequency and weighted by the measured power spectrum, for a QHS discharge at $\langle n_e \rangle = 2.0 \times 10^{12}$ cm^{-3}. The cross phases are distributed over a broad range at a given wave number (normalized to the local value of ρ_s). However, they are centered about a distinct average, shown by the dashed red line. The solid black line is a predicted n-φ cross phase spectrum determined using a linear kinetic electron drift wave theory [4]. The theory was applied using appropriate local plasma parameters determined from Thomson scattering measurements and geometry simplifications. The dominant contribution to the instability is from the trapped electron mode (TEM), due to the low collisionality ($\nu_{*e} \sim 0.1$) of these ECRH discharges. The measured cross phases are qualitatively similar with the linear TEM theory, with values near zero at $k_\theta = 0$ and increasing with wave number. This is in contrast to a 90° cross phase generally expected in resistive MHD theories. As an example, the dotted brown line in Fig. 4 is the predicted cross phase from a simplified resistive ballooning mode (BRM) instability estimate [5].

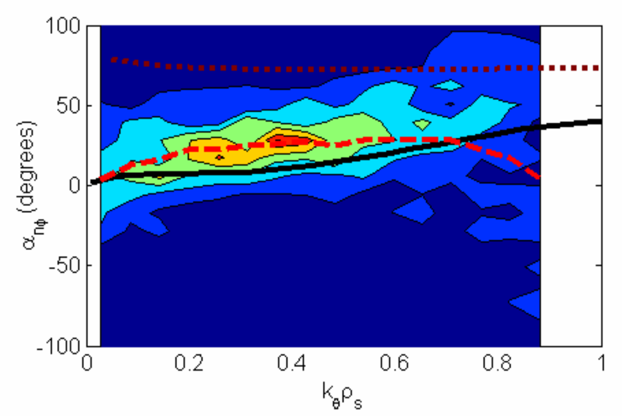

Fig. 4. Joint distribution of measured n-φ cross phase vs measured local k (normalized by ρ_s). The dashed red line is the average cross phase at a given wave number. The solid black and dotted brown lines are linear TEM [4] and RBM [5] instability estimates, respectively.

The measured fluctuation levels, spectra, and wave numbers have been used to infer, the turbulent driven electrostatic particle flux. Values on the order of 10^{15}–10^{16} cm^{-2}s^{-1} are found, comparable to values of particle flux inferred from H_α measurements and 3D DEGAS neutral gas simulations [6].

For additional comparison to theory, growth rates can be inferred from experimental data through the use of bispectral analysis [7]. Bispectra measure the coupling between three waves satisfying the condition $\vec{k} = \vec{k}_1 + \vec{k}_2$. If the turbulence is in steady state, and the linear growth of the underlying instability is balanced only by nonlinear three-wave interactions, then the measured non-linear energy transfer provides a measure of the linear growth rate spectrum. As it is typically not possible to measure 2D resolved turbulence in the laboratory, the above bispectral analysis is performed on frequency spectra measured at two poloidally separated locations. Frequencies are converted to k_θ through the use of Taylor's hypothesis with the measured phase velocities ($k_\theta = \omega/V_{\text{phase}}$).

Figure 5 shows the experimentally inferred growth rates for discharges in both the QHS and Mirror configurations at similar line-averaged densities. A region of damping is seen at the lowest wave numbers (frequencies). This coincides with the peak in the power spectra. Similar to the cross phases, the measured growth rates increase with increasing wave number. This is qualitatively similar to the linear growth rate spectrum predicted using Ref. [4], as shown by the solid black line in Fig. 5.

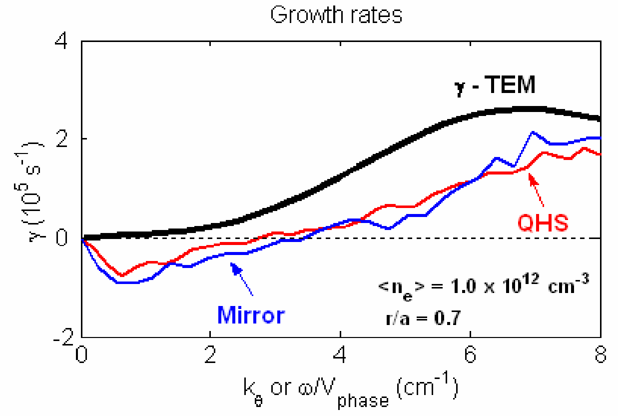

Fig. 5. Inferred linear growth rates for both the QHS and Mirror configurations. Also shown is the linear growth rate spectrum predicted from the electron drift wave theory [4].

Based on the turbulence measurements and approximate linear drift wave stability estimates, the TEM is a primary candidate for the cause of the anomalously large particle and electron thermal transport observed in HSX. To test the significance of the TEMs, predictive transport simulations have been carried out using theory-based models for both neoclassical transport [7] and ion temperature gradient (ITG)/TEM anomalous transport [9]. Although the axisymmetric ITG/TEM model of [9] cannot treat 3D geometry effects, recent 3D gyrokinetic linear stability calculations [10] have demonstrated the impact of the local geometry on ITG/TEM linear growth rates in stellarators. As an approximation to the results of Ref. [10], the largest value of local bad curvature in the low field/ballooning region of HSX is used in the evaluation of Ref. [9] (~3 × 1/R in HSX), with no free fit parameters. The model input particle and ECRH power source rates are determined from 3D neutral gas simulations and ray tracing calculations, respectively.

Figure 6 shows a comparison of the measured density and electron temperature profiles (from Thomson scattering) and the predicted profiles from the simulation for the QHS configuration at $\langle n_e \rangle = 1.5 \times 10^{12}$ cm^{-3}. Reasonable quantitative agreement is seen. In this simulation, the TEM accounts for the majority of the thermal and particle transport outside r/a ~ 0.2.

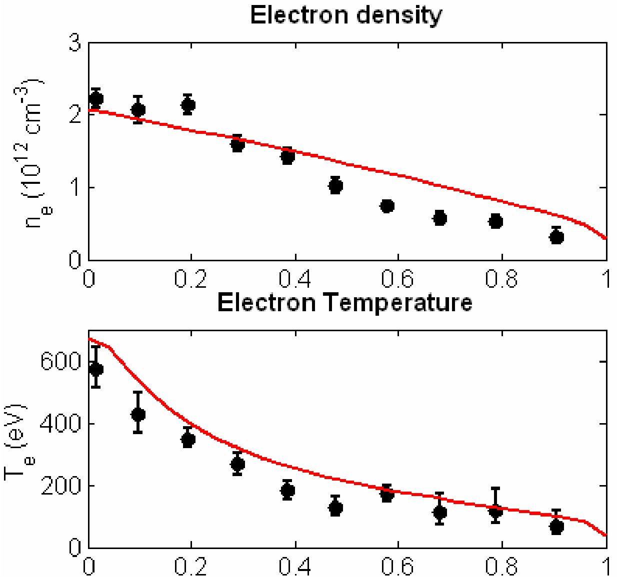

Fig. 6. Predicted density and electron temperature profiles in the QHS configuration using the ITG/TEM anomalous transport model [8]. Black dots are Thomson scattering measurements.

Walter Guttenfelder and the HSX Team
University of Wisconsin - Madison
Madison, WI 53706
E-mail: guttenfe@cae.wisc.edu

References

[1] J. M. Canik, 15th Stellarator Workshop, Madrid, Spain (2005).

[2] P. C. Liewer, Nucl. Fusion **25**, 543 (1985).

[3] J. M. Beall et al., J. Appl. Phys. **43**, 3993 (1982)

[4] W. Horton, Phys. Fluids **19**, 711 (1976).

[5] J. Callen, UW-CPTC report 05-9 (2005).

[6] J. M. Canik, 14th Stellarator Workshop, Greifswald, Germany (2003).

[7] J. S. Kim et al., Phys. Plasmas **3**, 3998 (1997).

[8] J. N. Talmadge et al., Fusion Sci. Technol. **46**, 255 (2004).

[9] H. Nordman et al., Nucl. Fusion **30**, 983 (1990)

[10] G. Rewoldt et al., Phys. Plasmas **12**, 102512 (2005).

Density regime of complete detachment and operational density limit in LHD

1. Introduction

The operational density range in a future magnetically confined deuterium-tritium fusion reactor will be of order 10^{20} m^{-3} [1, 2]. Higher density is more favorable as long as the confinement property is maintained, because the fusion reaction rate increases with the density squared. Furthermore, high-density operation aids in the achievement of detachment [3], which mitigates the divertor heat load to permissible values for realistic materials. The heat load is reduced because the edge plasma temperature decreases as a result of dilution cooling together with enhanced radiation and charge-exchange losses at high-density.

So-called Sudo density limit scaling [4] has often been used to discuss the operational density limit of helical plasmas. The Sudo scaling is defined by

$$n_c^{\mathrm{Sudo}}\ (10^{20}\ \mathrm{m}^{-3}) = 0.25\ [PB/(a^2R)]^{0.5},$$

where P (MW), B (T), a (m), and R (m) are the total heating power (P_{tot}), the magnetic field strength, the minor radius, and the major radius, respectively [4]. It should be noted that strongly peaked density profiles are not in the scope of the Sudo scaling. This scaling is based on the power balance between the heating power and the radiation loss that is proportional to n_e^2, where n_e is the electron density. In the Large Helical Device (LHD), radiative collapse is triggered even at a small radiation loss fraction of ~30%. Sustainable complete detachment, named the Serpens mode, has been found in LHD [5]. Complete detachment takes place when the electron temperature T_e at the last closed flux surface (LCFS) decreases to ~100 eV, or in other words, the hot plasma boundary $\rho_{100\mathrm{eV}}$ decreases to 1. Here, $\rho_{100\mathrm{eV}}$ is given by the normalized radius where T_e = 100±50 eV, and is larger than 1 in the attached phase. The reason that $\rho_{100\mathrm{eV}}$ is highlighted as the hot plasma boundary is explained in Section 3. The radiation loss fraction ranges from 30 to 100% at complete detachment [6]. It is therefore difficult to determine a threshold radiation loss fraction that triggers radiative collapse.

In this study, we experimentally investigate the operational density limit in LHD. Density regimes for complete detachment and the operational density limit in LHD are given in Section 2. In Section 3, edge plasma parameters are highlighted to discuss plasma behavior in the vicinity of operational density limit. A summary is given in Section 4.

2. Density regimes of complete detachment and radiative collapse

Pellet-fueled plasmas in LHD are characterized by strongly peaked density profiles. In gas-fueled plasmas, including completely detached plasmas, the density profile is hollow or flat. However, even in pellet-fueled plasmas, edge densities are similar to those in gas-fueled plasmas. In Fig. 1, $\langle n_e \rangle$ and the edge electron density, $n_e^{100\text{eV}}$, given by the electron density at $\rho_{100\text{eV}}$, are plotted against P_{tot} for neutral beam-heated plasmas at R = 3.65 m and B = 2.71 T. Shaded regions denote the density regimes for complete detachment. In Fig. 1, n_c^{Sudo} is calculated using fixed parameters of $a = a_0 = 0.64$ m, R = 3.65 m, and B = 2.71 T.

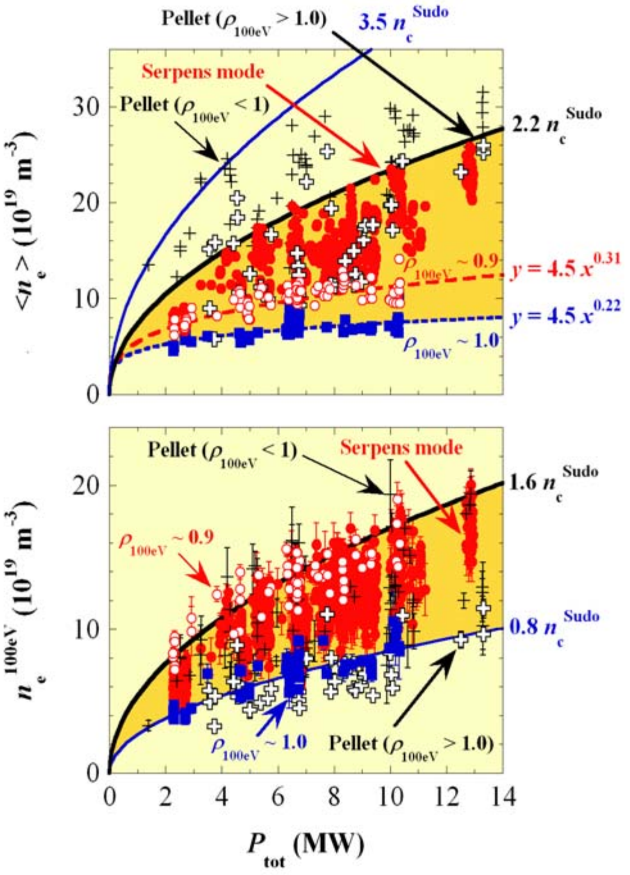

Fig. 1. The volume-averaged density (upper) and the edge density at the hot plasma boundary (lower) versus the total heating power.

High $\langle n_e \rangle$ reaching $2.2 n_c^{\text{Sudo}}$ is sustainable in Serpens mode plasmas. Higher $\langle n_e \rangle$ as high as 3.5 n_c^{Sudo} and the highest $\langle n_e \rangle$ of 3×10^{20} m^{-3} are achieved by applying pellet injection, although these are transient. Even in these pellet-fueled plasmas, however, the values of $n_e^{100\text{eV}}$ are similar to those obtained in gas-fueled plasmas. The high $\langle n_e \rangle$ achieved in pellet-fueled plasmas are a result of the strongly peaked density profiles.

3. Edge parameters

As mentioned in Section 1, the Sudo scaling is based on a power balance between P_{tot} and P_{rad} that is proportional to n_e^2, i.e., it is assumed that radiative collapse takes place at a critical radiation loss fraction of $P_{\text{rad}}/P_{\text{tot}} \propto n_e^2/P_{\text{tot}}$, and therefore, the critical density is proportional to $P_{\text{tot}}^{0.5}$. The large scatter of the radiation loss fraction, which ranges from 30 to 100% at detachment, suggests that this scenario is not sufficient to explain the density limit in LHD. However, the threshold edge density for complete detachment does increase with $P_{\text{tot}}^{0.5}$ (see Fig. 1), as predicted by the Sudo scaling. For a better understanding of this, we investigate the dependence of temperature on heating power and density.

Results of linear regression analysis of T_e for attached plasmas ($\rho_{100\text{eV}} > 1$) are summarized in Fig. 2, where the heating power and the density are scanned while the magnetic configuration is fixed to R = 3.65 m and B = 2.71 T. At each ρ, the local electron temperature, $T_e(\rho)$, is fitted by $n_e(\rho)^{\alpha n0}\, P_{\text{tot}}^{\alpha P0}$, or $n_e(\rho)^{\alpha n1}\, P_{\text{dep}}(\rho)^{\alpha P1}$, where $P_{\text{dep}}(\rho)$ is the total heating power deposited inside ρ, i.e., $P_{\text{dep}}(\rho = 1) = P_{\text{tot}}$. Use of P_{dep} is effective at taking into account the shallow penetration of heating beams in high-density plasmas. Since $P_{\text{dep}}(\rho) < P_{\text{tot}}$ inside the LCFS ($\rho < 1$), P_{tot} and $P_{\text{dep}}(\rho)$ give upper and lower estimates of the heating power, respectively. Note that $P_{\text{dep}}(\rho)$ is similar to P_{tot} in the outermost edge region $\rho > 0.9$, and therefore both fitting results coincide in this region. The ratio of $-\alpha P0/\alpha n0$ (or $-\alpha P1/\alpha n1$) is ~ 0.5 in the edge region and ~ 1 in the core region. This means that T_e can be expressed by a function of $(P_{\text{tot}}^{0.5}/n_e)$ in the edge region, while T_e in the core region is expressed by another function of (P_{tot}/n_e). For example, T_e at ρ = 1 is well fitted by $(P_{\text{tot}}^{0.5}/n_e)^{2/3}$, as is shown in Fig. 3. This fitting fails, however, at T_e < 100 eV, suggesting that the heating power is lost by an enhanced radiation in the low temperature regime, and/or the transport property changes. Although the reason why this occurs at T_e ~ 100 eV is not known and remains for future studies, the critical temperature shows almost no dependence on P_{tot} [7], at least under fixed experimental conditions of magnetic configuration, working gas, and wall conditioning.

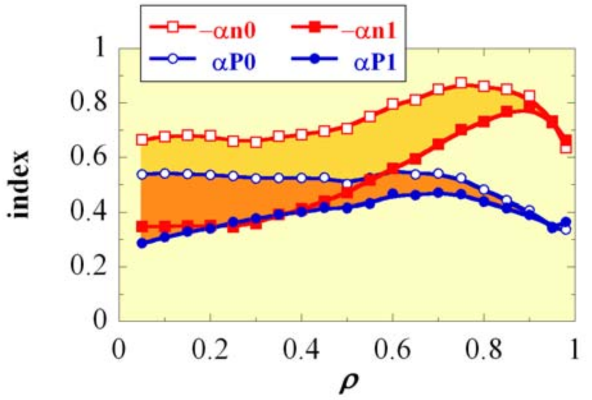

Fig. 2. Summary of regression analysis of the electron temperature in attached plasmas. See text for definition of fitting parameters.

Since the edge temperature is a function of $P_{\text{tot}}^{0.5}/n_{\text{e}}$, the critical density that results in a critical temperature should be dependent on $P_{\text{tot}}^{0.5}$ as seen in Fig. 1 and in the Sudo scaling. In this explanation, the power balance between P_{tot} and P_{rad} is not mentioned explicitly. Nevertheless, this power balance might be playing an important role in determining the critical temperature.

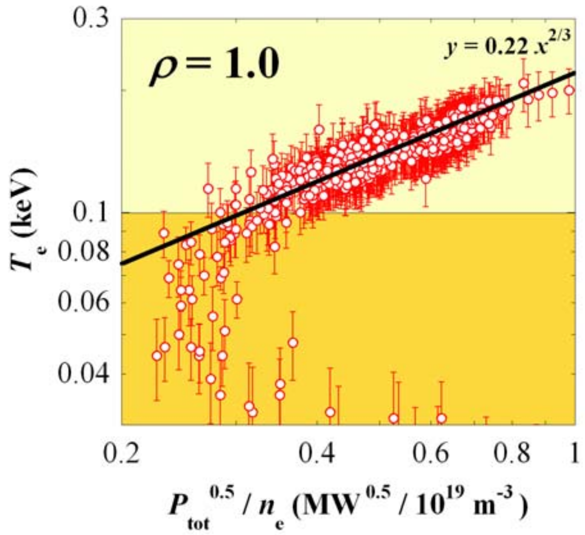

Fig. 3. Electron temperature dependence on the square root of heating power divided by the local electron density, at the LCFS.

At complete detachment, $n_{\text{e}}^{100\text{eV}}$ begins to increase rapidly, reflecting improvement of the effective fueling efficiency, and continues to increase toward radiative collapse, unless gas fueling is decreased [5]. However, this increase of the edge density is only observed inside $\rho_{100\text{eV}}$. Outside the hot plasma boundary ($\rho > \rho_{100\text{eV}}$), the density decreases as the plasma column shrinks, even though gas fueling is continued. Figure 4 shows $n_{\text{e}}(\rho) / P_{\text{tot}}^{0.5}$ at fixed positions of $\rho = 0.8$, 0.9, and 1.0, in shrinking plasmas with $R = 3.65$ m and $B = 2.71$ T, where $\rho_{100\text{eV}}$ decreases from >1 to zero (from right to left, in Fig. 4). The local density at each ρ increases with decreasing $\rho_{100\text{eV}}$, as long as $\rho_{100\text{eV}} > \rho$, and begins to decrease with $\rho_{100\text{eV}}$ after $\rho_{100\text{eV}}$ passes through ρ. As a result, for example, the maximum density at $\rho = 0.9$ is obtained when $\rho_{100\text{eV}} \sim 0.9$, i.e., the maximum of $n_{\text{e}}(0.9)$ is roughly equal to $n_{\text{e}}^{100\text{eV}}$ at $\rho_{100\text{eV}} = 0.9$. Therefore, $n_{\text{e}}^{100\text{eV}}$ is a good representative of the maximum of $n_{\text{e}}(\rho)$ at each ρ. Now the meaning of $\rho_{100\text{eV}}$ as the hot plasma boundary can be redefined: $\rho_{100\text{eV}}$ is the radial position inside which the electron density can be increased by fueling.

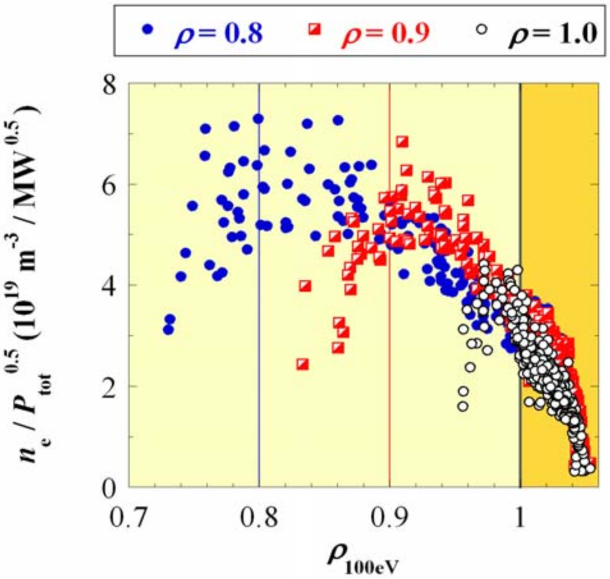

Fig. 4. Local densities normalized by the square root of total heating power, with respect to the hot plasma boundary.

Since $n_{\text{e}}^{100\text{eV}}$ represents the maximum local density and increases with $P_{\text{tot}}^{0.5}$, a plot of $n_{\text{e}}^{100\text{eV}}/P_{\text{tot}}^{0.5}$ versus $\rho_{100\text{eV}}$, as in Fig. 5, gives a radial profile of maximum edge densities in attached and detached plasmas. The maximum edge density increases as the plasma column shrinks and $\rho_{100\text{eV}}$ decreases. In the attached condition ($\rho_{100\text{eV}} \geq 1$), therefore, the maximum is reached at $\rho_{100\text{eV}} = 1$, which roughly corresponds to 0.8 $n_{\text{c}}^{\text{Sudo}}$ on average. In the case of Fig. 5, $n_{\text{c}}^{\text{Sudo}}$ is calculated using $a = \rho_{100\text{eV}} a_0$, to take into account the shrinking minor radius, while $R = 3.65$ m and $B = 2.71$ T are fixed. As $\rho_{100\text{eV}}$ decreases, the maximum edge density increases further and then saturates at ~1.5 $n_{\text{c}}^{\text{Sudo}}$ at $\rho_{100\text{eV}} \leq 0.95$. Even in pellet-fueled plasmas (crosses in Fig. 5), the maximum edge density follows the same tendency as in gas-fueled plasmas (open circles).

Note that this maximum edge density is not necessarily sustainable. To avoid further shrinking that leads to radiative collapse, one should decrease the fueling. The Serpens mode appears in such a situation (closed circles). In the Serpens mode phase, $\rho_{100\mathrm{eV}}$ fluctuates within 0.8 to 0.95, and correspondingly, the maximum edge density also fluctuates within 1.5 n_c^{Sudo} to 0.8 n_c^{Sudo}. Even if the edge density decreases to 0.8 n_c^{Sudo}, which is the threshold density for complete detachment, the Serpens plasma keeps the detachment condition of $\rho_{100\mathrm{eV}} < 1$. At a low recycling condition, however, the plasma does reattach after the Serpens mode phase.

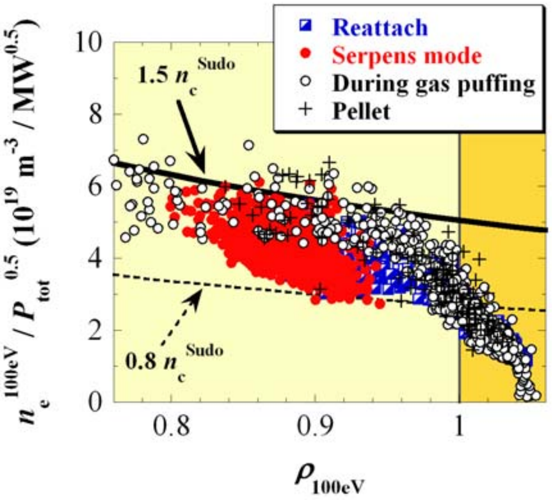

Fig. 5. Relation between the shrinking hot plasma boundary and the edge electron density, normalized by the square root of total heating power.

4. Summary

High volume-averaged density of 3.5 times as high as the Sudo scaling has been achieved using pellet injection in LHD, where the density profile is strongly peaked. Even in these pellet-fueled plasmas, the edge densities are similar to those in gas-fueled plasmas. Complete detachment in LHD takes place when the edge temperature at LCFS decreases to a critical value of ~100 eV. In the edge region, the electron temperature is a function of the square root of the heating power divided by the electron density. Consequently, the critical edge density that results in complete detachment is proportional to the square root of the heating power, as expressed in the Sudo density limit scaling. The critical edge density roughly corresponds to 0.8 times the Sudo scaling. High volume-averaged densities reaching ~2.2 times the Sudo scaling are sustainable in the Serpens mode plasmas, where the edge density is limited to ~1.5 times the Sudo scaling. Fueling and recycling control is necessary to reproduce the Serpens mode, because an excess (a shortage) of neutral pressure leads to radiative collapse (reattachment).

A fuller description of this topic will be presented as paper EX/3-2 at the forthcoming 21st IAEA Fusion Energy Conference in Chengdu, China.

Junichi Miyazawa
National Institute for Fusion Science
Toki, Gifu 509-5292, Japan
E-mail: miyazawa@LHD.nifs.ac.jp

References

[1] J. D. Lawson, Proc. Phys. Soc. (London) **B70** (1957) 6.

[2] A. Sagara et al., Nucl. Fusion **45** (2005) 258.

[3] C. S. Pitcher and P.C. Stangeby, Plasma Phys. Control. Fusion **39** (1997) 779.

[4] S. Sudo et al., Nucl. Fusion **30** (1990) 11.

[5] J. Miyazawa et al., Nucl. Fusion **46** (2006) 532.

[6] J. Miyazawa et al., Plasma Fusion Res. **1** (2006) 026.

[7] B. J. Peterson et al., "Characteristics of Density Limiting Radiative Collapse in the Large Helical Device," Plasma Fusion Res. (submitted).

NCSX component production hits its stride

The National Compact Stellarator Experiment (NCSX) construction project has reached the halfway point and is currently focused on the fabrication of major components: the modular coils, the vacuum vessel, and the toroidal field coils. The NCSX is a major initiative of the U.S. Department of Energy's Fusion Energy Sciences program. Its mission is to study the physics of compact stellarators for fusion energy and to advance three-dimensional (3D) plasma physics. The project is led by Princeton Plasma Physics Laboratory (PPPL), the host site, in partnership with Oak Ridge National Laboratory. Progress in component production has been marked by several significant accomplishments in recent months, with components now being produced and delivered at a steady rate, consistent with the July 2009 target for project completion.

In July 2006, the project took delivery of the eighth modular coil winding form (MCWF), the sixth in as many months. The MCWFs are stainless steel castings with accurately machined surfaces that control the geometry of the coils during winding and assembly. Each modular coil (Fig. 1) is mounted on its own winding form, which stays with the coil after winding and is installed on the machine as part of the permanent support structure. The eighteen forms, six each of three different shapes, are being manufactured by a team of companies led by Energy Industries of Ohio, Inc. (EIO) of Independence, Ohio. In June, foundry partner MetalTek International of Pevely, Missouri, shipped the eighteenth and final casting to the machining partner, Major Tool and Machine, Inc., (MTM) of Indianapolis, Indiana. The coils' complex geometries and tight tolerances (±0.020 in.) are technically challenging, and MTM devoted a substantial and ultimately successful effort over many months to develop an efficient machining process that meets the project's technical specifications. After the third form was delivered in February 2006, subsequent units have been delivered at a rate of about one per month, consistent with the project's schedule.

Fig. 1. Completed modular coil.

Fabrication of the first modular coil was completed in March 2006. The coils are being fabricated at PPPL using a flexible copper rope conductor wound on the MCWF winding surfaces. The winding pack is a complex assembly that includes the conductor, glass and Kapton insulation, and copper cooling elements, all encapsulated in epoxy. The fabrication processes were developed through a series of R&D tasks, including the construction and testing of a prototypical coil, before starting production. The method that was developed for achieving the required ±0.020 in. tolerance on the position of the current center takes advantage of the flexible conductor, which allows small adjustments in the pack dimensions to be made after winding, eliminating the need for shims.

The current center position is inferred from coordinate measurements of the winding form and conductor that are made with a portable coordinate measuring arm. Temporary winding clamps are set to predetermined positions before winding, based on measurements of the winding surface. After winding, the completed winding pack dimensions are measured and, if necessary, adjusted using the clamps to put the current center in the required location. Overall, the developed process was successfully applied in the manufacture of the first coil. Follow-up testing revealed a localized insulation weakness in the lead area, which was fully corrected with a minor design modification, after which the coil passed final manufacturing acceptance tests. As of August 2006, four modular coils have been fabricated and tested.

The first two NCSX vacuum vessel segments (Fig. 2) were delivered in May and July 2006, respectively. The third and last segment is due for delivery in September. The segments and the accompanying port extensions are fabricated by MTM. The identical segments are constructed of formed 0.375-in.-thick Inconel panels. The panels are welded together to form a shell with a complex shape similar to that of the enclosed plasma, and then vacuum tested. The tolerance on the finished shell geometry is ±0.188 in. The ports will be installed by PPPL during the subassembly process, and the three segments will be joined to form a complete torus during final machine assembly.

Fig. 2. Vacuum vessel segment with ports attached for testing.

Another recent milestone was the award in May 2006, of a $1.5M contract for the (planar) toroidal field coils to Everson Tesla, Inc., of Nazareth, Pennsylvania. Currently, tooling and facility preparations are in progress, with the first coil scheduled for delivery in February 2007.

The NCSX construction project began in April 2003, and the contracts for the modular coil winding forms and the vacuum vessel, the two largest contracts, were awarded in September 2004. The project, now just past the half-way point, is on schedule for completion in July 2009. Modular and toroidal field coil fabrication will continue throughout 2007. Subassembly activities have begun and will continue through 2008 as more finished components become available. The device will be installed, adapted to power supplies and controls, and tested by creating a first plasma in 2009.

G. H. Neilson
Princeton Plasma Physics Laboratory
P.O. Box 451
Princeton, NJ 08543-0451
E-mail: hneilson@pppl.gov

Stellarator reactor design lecture presentation materials available

Horst Wobig held a series of tutorial seminars on the Stellarator Reactor in Greifswald. Materials presented during the series are available via the W7 Seminar home page (select talks 2006 in the right-hand menu):

http://w7x.info/w7seminar/w7is_w7sem.html

To access the site, login as user *w7as_team*, with password *stella*.

Note that you will find the transparencies, the software for coil optimization, and more materials on the stellarator reactor also via the home page of Stellarator System Studies:

http://w7x.info/proj_sss/w7is_proj_sss.html

Thanks to Herrn Wobig, Herrn Harmeyer, and A. Dinklage who helped with providing this material.